

## UNDERSTANDING WHY THE COMBINATION OF ACIDIZING AND HYDRAULIC FRACTURING CAN ACTUALLY BE SUCCESSFUL

*Data de aceite: 02/06/2023*

**Henrique Toby Ribeiro**  
3R Petroleum

**José Maria Júnior Santos**  
Universidade Federal de Minas Gerais

**Humberto Almeida Oliveira**  
Universidade Federal de Minas Gerais

**ABSTRACT:** The combination of acidizing and hydraulic fracturing seems to be a very logical approach to achieve the maximum stimulated volume in unconventional reservoirs. However, this hybrid technique is not yet widely used due to the notion that acidizing could compromise the mechanical integrity of the rock and affect fracture conductivity. This paper delves into the analysis of microscopic images of acidized carbonate and siltstone specimens, coupled with nanoindentation analysis and proppant embedment tests to better understand acid-proppant fracturing.

**KEYWORDS:** Acid Propped Fracturing, Proppant Embedment, Unconventional Reservoir, Nanoindentation, Fracture Conductivity.

### 1 . INTRODUCTION

The idea of combining hydraulic fracturing and acid stimulation, or acid-proppant fracturing, was patented in the last century by Cardwell et al. (1957). But the first well-known field cases of acid-proppant fracturing didn't happen until 2010.

The study presented here is based on the characterization of three types of rocks from the Neoproterozoic section of the São Francisco Basin: a crystalline limestone, a microbial or biogenic carbonate (stromatolite) and a siltstone. The São Francisco Basin is an unconventional gas reservoir approximately 600 Ma years old located in the central part of Brazil (Vieira et al., 2007; Uhlein et al., 2017).

Microscopic analysis of acidized specimens revealed two types of neolayers resulting from acid-rock interaction. The mechanical properties of the neolayers were evaluated using the nanoindentation technique and proppant embedment tests were performed to compare acidized and non-acidized specimens.

## 2 . METHODS AND MATERIALS

### 2.1 Compositional analysis

A detailed compositional analysis was performed for each of selected the rock types from the San Francisco Basin.

Table 1 presents the chemical analysis given by x-ray fluorescence (XRF), Table 2 presents the mineralogical analysis given by x-ray diffraction (XRD) and Table 3 presents the total organic carbon (TOC) analysis.

The analyses revealed that the limestone samples were practically pure calcite, while stromatolite, a carbonate of microbial origin, showed a higher quartz content compared to limestone. The siltstone samples contained mainly silica and aluminum silicates.

Table 1. Total  $CaCO_3$ , total sulfur and XRF analysis.

Rock	LOI Total $CaCO_3$	Direct Combustion Total Sulfur (%)	X-Ray Fluorescence (%)				
			$Al_2O_3$	CaO	$Cr_2O_3$	$Fe_2O_3$	$K_2O$
Siltstone	2.96	0.04	12.37	1.4	<0.01	5.13	2.66
Stromatolite	40.44	0.01	0.34	49.91	<0.01	0.12	0.14
Limestone	43.20	0.03	<0.1	55.68	<0.01	0.1	0.01

Rock	X-Ray Fluorescence (%)						
	MgO	MnO	$Na_2O$	$P_2O_5$	$SiO_2$	$TiO_2$	-
Siltstone	2.08	0.08	2.88	0.21	69.26	0.84	-
Stromatolite	0.38	0.01	<0.1	0.04	8.51	0.01	-
Limestone	0.12	0.01	<0.1	0.12	0.66	0.01	-

**Source:** produced by the authors.

Table 2. XRD Analysis.

Rock	X-Ray Diffraction (%)				
	Calcite	Quartz	Muscovite	Albite	Chamosite
Siltstone	4.5	41.1	17.6	26.2	10.6
Stromatolite	91.5	8.5	-	-	-
Limestone	99.3	0.7	-	-	-

**Source:** produced by the authors.

Table 3. Total Organic Carbon (TOC) Analysis.

Rock	Organic carbon(%)	Graphite (%)	Inorganic carbonate (%)
Siltstone	<0.05	0.06	<0.05
Stromatolite	<0.05	0.17	10.97
Limestone	<0.05	0.12	11.47

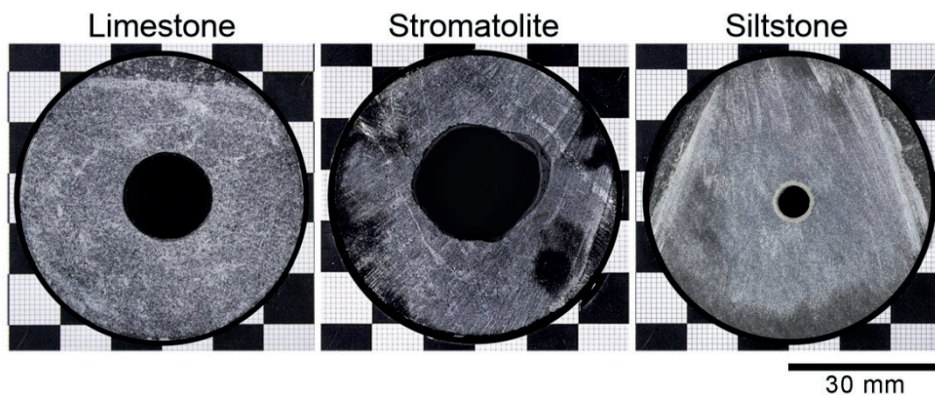
**Source:** produced by the authors.

## 2.2 Acid etching experiment

The core samples were prepared with a central hole of 0.60 cm in diameter for the acid injection. During the acidizing procedure, the samples were positioned in a vertical position and 900 ml of 15% hydrochloric acid (HCl) were pumped from bottom to top inside the orifice at 15 mL/min, atmospheric pressure and laboratory temperature (22 °C). In this dynamic test, the CO<sub>2</sub> bubbles moved continuously away from the rock surface and the contact between the acid and the rock surface was not impaired.

The sections displayed in Figure 1 were cut at 1.00 cm from the acid injection point. They show the dissolution results for the three different lithofacies. The stromatolite showed the highest dissolution rate, while the siltstone showed only a bleached layer, visible by naked eye.

**Figure 1** – Rock dissolution results after 15% hydrochloric acid was injected inside the rock cores.



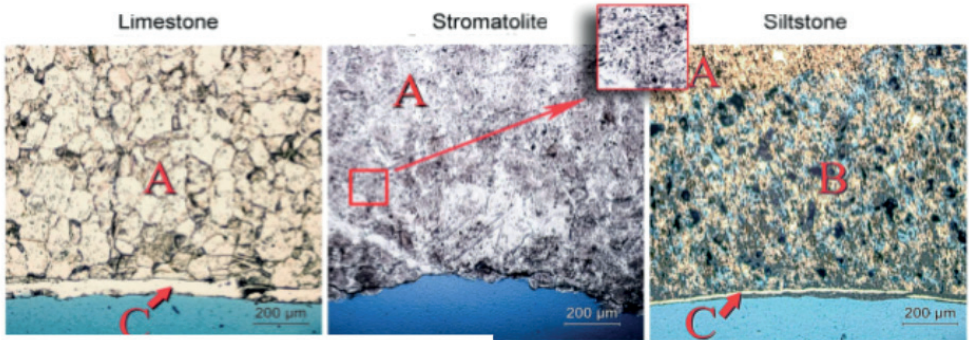
**Source:** produced by the authors.

## 2.3 Petrographic thin sections and resin mounted specimens

For the preparation of the petrographic thin sections and resin-mounted specimens, the acidized holes in Figure 1 were filled with a blue resin in order to preserve the microstructures originated during the acid etching process.

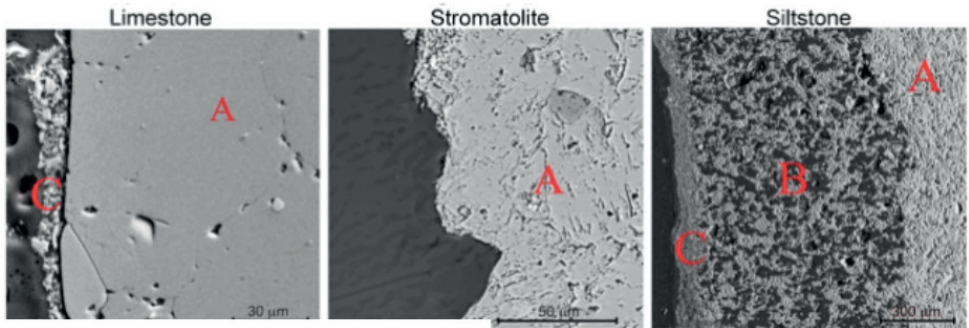
The petrographic thin sections were analyzed with optical microscopy, Figure 2, and the resin mounted specimens were analyzed with scanning electronic microscope (SEM), Figures 3 and 4.

**Figure 2** - Microphotography showing the original rock matrices (A) and the neolayers resulting from the acidizing process (B and C). Note the microposity of the stromatolite highlighted on top.



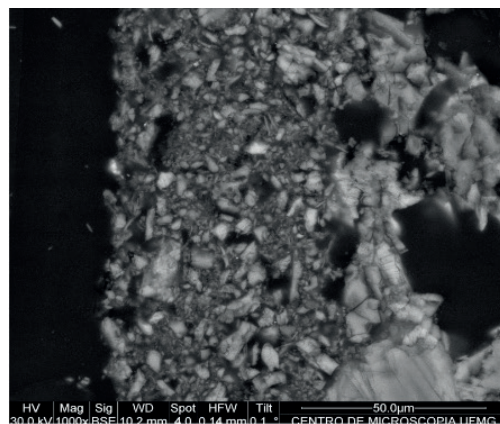
**Source:** produced by the authors.

**Figure 3** - SEM images of the neolayers B and C discovered on top of the original rock matrices (A).



**Source:** produced by the authors.

**Figure 4** - Detailed SEM image of neolayer C in the siltstone.



**Source:** produced by the authors.

## 2.4 Proppant embedment specimen's preparation

The specimens for the proppant embedment tests were prepared with a diameter of 9.80 cm, a height of 4.00 cm and were mechanically rectified to achieve smooth flat surfaces. Then, half of the specimens had one of the flat sides acidized (Figure 5) in order to perform comparative embedment proppant tests between acidized and non-acidized specimens.

**Figure 5:** Acidized specimens prepared for the proppant embedment tests. The asperities in the stromatolite are far more evident.



**Source:** produced by the authors.

The acidification procedure for the above samples consisted of immersing one of the rectified flat sides in 300 ml of 15% HCl solution for period of 1 hour in a pressurized cell at 100 psi pressure.

## 3 . THEORY

### 3.1 Nanoindentation

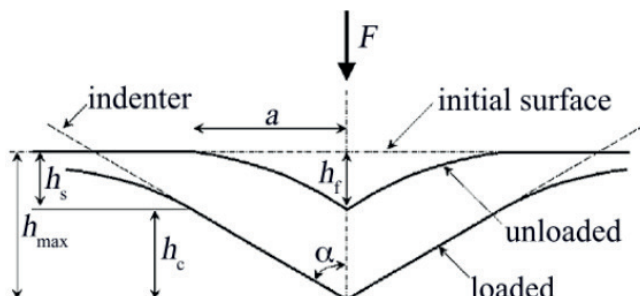
Nanoindentation analysis has been used to characterize mechanical properties of different materials, such as metal alloys, polymers, thin films, biological tissues and cement-based materials (Liu et al., 2018).

Nanoindentation has also been used to study the mechanical properties of shale formations and optimize hydraulic fracturing designs (Kumar et al., 2012).

The theoretical basis of nanoindentation was established by Oliver and Pharr (1992), and generally this process can be carried out either on a constant loading rate (CLR) mode or on a constant strain rate (CSR) mode. The majority of nanoindentation studies in shale are performed using the CLR mode, where the maximum load needs to be pre-determined and deeper indentation depths indicate inferior mechanical properties (Shi et al., 2020).

Figure 6 illustrates the nanoindentation process. The indentation depth ( $h_{max}$ ) corresponds to the vertical surface deflection at the perimeter of contact ( $h_s$ ) plus the contact depth ( $h_c$ ).

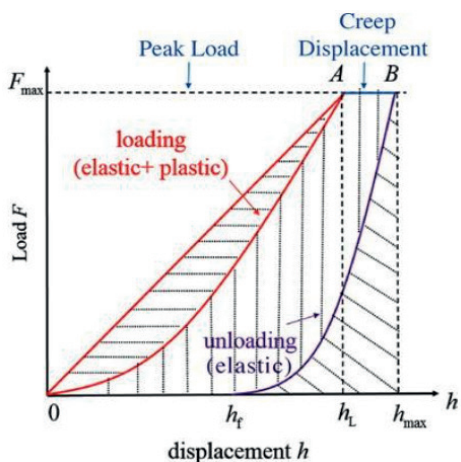
**Figure 6** - Schematic cross-section of a nanoindentation process.



**Source:** produced by the authors.

Figure 7 illustrates the load vs. displacement curve which consists of three stages: loading, holding, and unloading.

**Figure 7** - Load vs. displacement nanoindentation curve.



**Source:** produced by the authors.

The loading stage is a combination of elastic and plastic deformation, while the unloading stage consists of elastic (recovered) deformation.

The holding stage, also called creep displacement (Li et al., 2019), is used to study creep behavior of the rock (Liu et al., 18).

### 3.2 Proppant embedment, proppant pack compaction and fracture conductivity

Proppant embedment and proppant pack compaction are considered to play the primary roles in fracture width loss (Guo et al., 2017; Chen et al., 2017). The proppant pack compaction also leads to a loss of porosity and permeability of the proppant pack (Neto et al., 2015). Width and permeability losses result in the decrease of fracture conductivity according to Equation 1:

$$F_c = K_f \times w_f \quad (1)$$

where  $F_c$  is the fracture conductivity,  $k_f$  is the proppant pack permeability and  $w_f$  is the fracture width.

The proppant pack permeability can be calculated by the empirical Carman-Kozeny equation, Equation 2, widely used to predict the permeability of random sphere packs (Sanematsu et al., 2015).

$$k_f = \frac{d_p^2 \phi^3}{180(1-\phi)^2} \quad (2)$$

where  $d_p$  is the median proppant diameter and  $\phi$  is the porosity of the proppant pack that can be calculated by Equation 3 (Neto et al., 2015):

$$\phi = \frac{V_p}{V_b} = 1 - \frac{V_s}{V_b} \quad (3)$$

where  $V_p$  is the volume of the porous space within the prop-pant pack,  $V_s$  is the volume of the solid proppant particle, and  $V_b$ , expressed by Equation 4, is the bulk volume of the proppant pack:

$$V_b = V_p + V_s \quad (4)$$

In general, the proppant embedment represents the main part of fracture width loss, while the proppant pack compaction plays a secondary role (Gao et al., 2013). The factors that have a greater influence in the proppant embedment are related to the characteristics of the formation (clay content, total organic carbon, porosity of formation, carbonate and quartz content) and proppant characteristics (proppant type, size, proppant distribution, concentration, and number of layers) (Bandara et al., 2019).

Guo et al. (2012) proposed an analytical model that incorporated both elastic and creep deformation in the proppant embedment model to analyze how time influences proppant embedment, assuming tightly packed and non-deformable proppants.

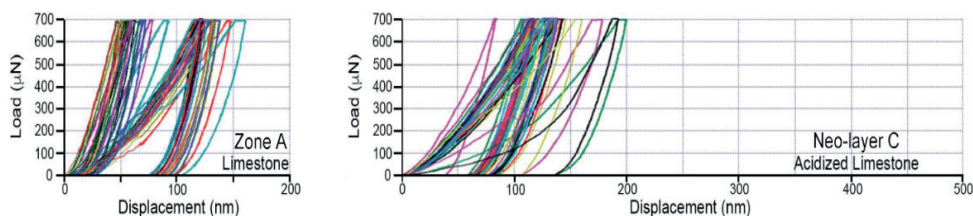
According to Guo et al. (2012), in a first stage, the proppant instantly embeds at a certain depth into the rock replicating the elasticity theory. Then in a second stage of creep deformation, the proppant continues to embed slowly and constantly simulating the viscoelastic theory.

## 4 . EXPERIMENTS AND RESULTS

### 4.1 Nanoindentation tests

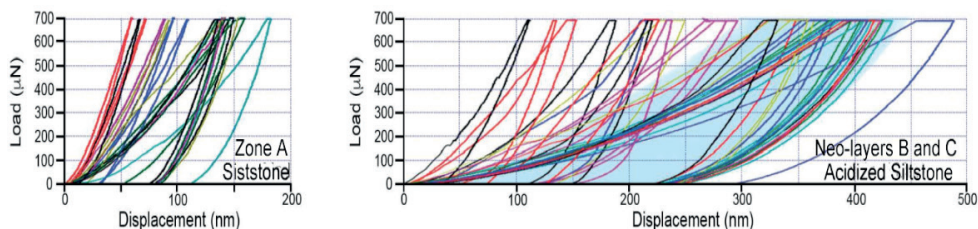
Nanoindentation tests were carried out using a Berkovich indenter at a constant loading rate of  $70 \mu\text{N/s}$  and a maximum load of  $700 \mu\text{N}$  maintained at peak load for 10 s. The indentation points were located at the vertices of a  $50 \times 50 \mu\text{m}$  grid. The neolayers B and C presented deeper indentation depths compared to the original rock matrices, confirming the weakening of the surface properties of the rock as a result of acid etching (Figure 8 and Figure 9).

**Figure 8** - Load-depth curves for the non-acidized limestone (Zone A, on the left side) and its respective neolayer C (right).



**Source:** produced by the authors.

**Figure 9** - Load-depth curves for the non-acidized siltstone (Zone A, on the left side), and neolayers B and C (right). The blue region is the indentation range of the blue resin that fills the voids in neolayer B.

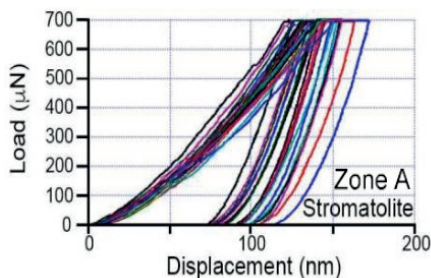


**Source:** produced by the authors.

The siltstone was the type of rock mostly affected by acid etching. The curves associated with neolayers B and C (Figure 9) reached indentation depths of up to 500 nm and showed large creep displacements related to the decrease in Young's modulus and hardness (Liu et al., 2018).

The stromatolite was the only lithofacies that did not present neolayers and the indentation depths for the stromatolite (Figure 10) revealed it had poorer mechanical properties when compared to the non-acidized specimens of limestone and siltstone, but better mechanical properties when compared to the acidized specimens of limestone and siltstone.

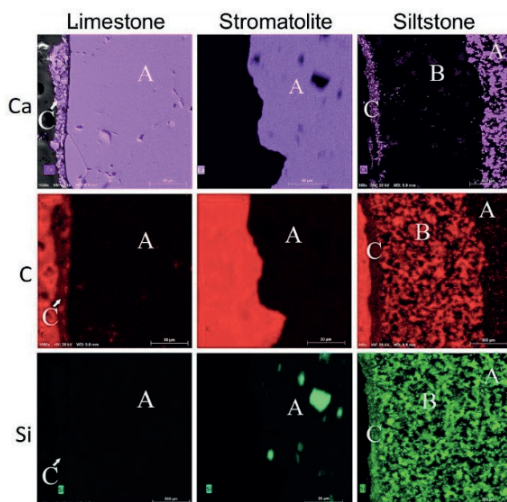
**Figure 10** - Load-depth curves for the non-acidized stromatolite (Zone A).



**Source:** produced by the authors.

In Figure 11 below, it is possible to observe the zone of acid invasion in the siltstone, and the composition of the residual (B) and recrystallization (C) neolayers provided by energy-dispersive X-ray spectroscopy (EDS). The C neolayer in limestone consists exclusively of calcite crystals (top-left), while in siltstone it is made up of calcite and insoluble silicate grains that were “captured” during the calcite recrystallization process (top-right and bottom-right). Neolayer B is made up exclusively of silicates (bottom-right) and the carbon of the resin applied to the samples can be seen filling the voids left by the calcite removed from the acid invasion zone B (middle-right).

**Figure 11** - EDS mapping for calcium, carbon, and silicon.



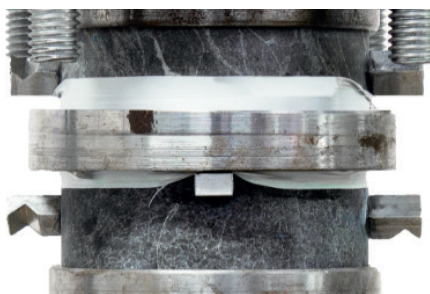
**Source:** produced by the authors.

## 4.2 Proppant embedment tests

The proppant embedment tests used 20/40 high strength bauxite ( $425\text{-}850\ \mu\text{m}$ ) at  $10.00\ \text{Kg/m}^2$ , for 8 hours under a pressure of 40 MPa (5800 psi).

Proppant embedment values were determined by subtracting the total axial compression measured in the experimental assembly shown in Figure 12, from the specific axial compressions of the rock waffles and of the proppant pack; both determined separately in a series of previous experiments using analog samples and under identical conditions.

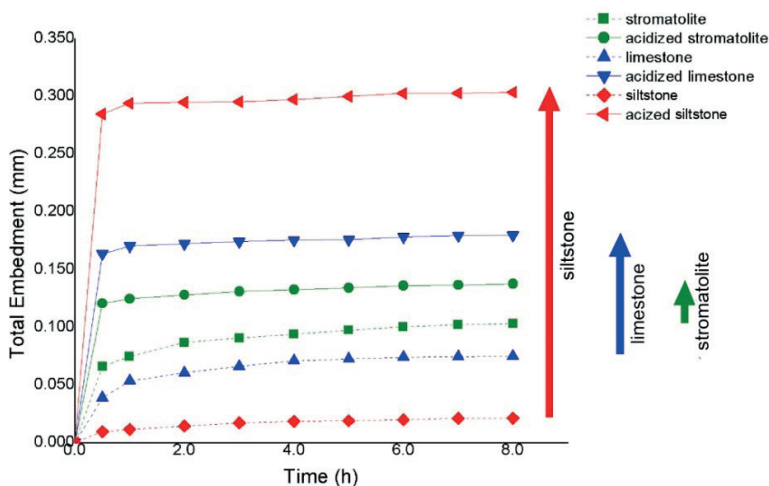
**Figure 12** - Proppant embedment experimental assembly.



**Source:** produced by the authors.

As expected, the siltstone, with the thickest set of neolayers, presented the highest increment in proppant embedment. On the other hand, the stromatolite, not having any type of neolayers, presented the minimum increment in terms of proppant embedment. Finally, the limestone, containing only the recrystallization neolayer (Zone B), presented an intermediary increment situated between those observed in the siltstone and in the stromatolite (Figure 13).

**Figure 13** - Proppant embedment results for acidized and non-acidized specimens.



**Source:** produced by the authors.

## 5 . CONCLUSIONS

A cautious analysis of the results presented in this article may explain why acid-proppant fracturing, which is a combination of acid stimulation and hydraulic (propped) fracturing, can exceed the results of each of the stimulation techniques applied individually.

Two types of neolayers resulting from acidizing were discovered: a residual and a recrystallization type. The residual neolayer was observed only in the siltstone which is rich in quartz and aluminum silicates. The recrystallization neolayer was observed both in the limestone and to a lesser extent in the siltstone which presented some calcium carbonate content.

The stromatolite was the only type of rock that did not present any neolayer. Probably because the amount of silicates was not high enough to allow the existence a residual neolayer and probably because a turbulent dissolution interface prevented the reprecipitation of calcium carbonate crystals as the stromatolite clearly showed the highest dissolution rate.

When neolayers are not present, it is very unlikely that acidizing could be contributing to the increased in proppant embedment, but it will certainly be contributing to the increase of reservoir's permeability beyond the propped fracture. And when the neolayers are present, as a result of acidizing, their contribution to fracture conductivity loss tends to be very limited due to the small thickness associated with the neolayers.

Further testing with different types of reservoir rocks under various pressure and temperature conditions is a suggestion for future work to allow the generalization of the rules determining the presence and characteristics of neolayers.

## 6 . REFERENCES

Bandara, K., et al., 2019. Improved understanding of proppant embedment behavior under reservoir conditions: A review study. **Powder Technology**.

Cardwell, P.H., et al., 1957. **Well treatment**. US Patent 2,802,531.

Chen, D., et al., 2017. A permeability model for the hydraulic fracture filled with proppant packs under combined effect of compaction and embedment. **Journal of Petroleum Science and Engineering** 149, 428–435.

Gao, Y., Lv, Y., Wang, M., Li, K., 2013. New mathematical models for calculating the proppant embedment and conductivity, in: IPTC 2013: **International Petroleum Technology Conference**, European Association of Geoscientists & Engineers. pp. cp–350.

Guo, J., et al., 2012. Modeling of proppant embedment: elastic deformation and creep deformation, in: SPE **International Production and Operations Conference & Exhibition**, Society of Petroleum Engineers.

Guo, J., et al., 2017. Analytical analysis of fracture conductivity for sparse distribution of proppant packs. **Journal of Geophysics and Engineering** 14, 599–610.

- Kumar, V., et al., 2012. Estimation of elastic properties of organic matter in Woodford shale through nanoindentation measurements, in: **SPE Canadian Unconventional Resources Conference**, Society of Petroleum Engineers.
- Li, C., et al., 2019. Indentation creep behavior of Fe-based amorphous coatings fabricated by high velocity oxy-fuel. **Journal of Non-Crystalline Solids** 503, 62–68.
- Liu, K., et al., 2018. Application of nanoindentation to characterize creep behavior of oil shales. **Journal of Petroleum Science and Engineering** 167, 729–736.
- Neto, L.B., et al., 2015. Conductivity and performance of hydraulic fractures partially filled with compressible proppant packs. **International Journal of Rock Mechanics and Mining Sciences** 74, 1–9.
- Oliver, W.C., Pharr, G.M., 1992. An improved technique for determining hardness and elastic modulus using load and displacement sensing in- dentation experiments. **Journal of materials research** 7, 1564–1583.
- Sanematsu, P., et al., 2015. Image-based stokes flow modeling in bulk proppant packs and propped fractures under high loading stresses. **Journal of Petroleum Science and Engineering** 135, 391–402.
- Shi, X., et al., 2020. Application of nanoindentation technology for characterizing the mechanical properties of shale before and after supercritical CO<sub>2</sub> fluid treatment. **Journal of CO<sub>2</sub> Utilization** 37, 158–172.
- Uhlein, G.J., et al., 2017. Early to late Ediacaran conglomeratic wedges from a complete foreland basin cycle in the southwest São Francisco craton, Bambuí group, Brazil. **Precambrian Research** 299, 101–116.
- Vieira, L.C., et al., 2007. A formação Sete Lagoas em sua área-tipo: fácies, estratigrafia e sistemas deposicionais. **Revista Brasileira de Geociências** 37, 1–14.

## 7 . ACKNOWLEDGEMENTS

The authous would like to acknowledge the support of CNPq, UFMG and Centro de Microscopia (UFMG).